



Quantitative phase imaging of stromal prognostic markers in pancreatic ductal adenocarcinoma

MICHAEL FANOUS,^{1,2} ADIB KEIKHOSRAVI,³ ANDRE KAJDACSZY-BALLA,⁵ KEVIN W. ELICEIRI,^{3,4}  AND GABRIEL POPESCU^{1,2,*}

¹Department of Bioengineering, University of Illinois at Urbana-Champaign, Urbana, IL 61801, USA

²Quantitative Light Imaging Laboratory, Beckman Institute for Advanced Science and Technology, University of Illinois at Urbana-Champaign, Urbana, IL 61801, USA

³Laboratory for Optical and Computational Instrumentation, Department of Biomedical Engineering, University of Wisconsin, Madison, WI 53706, USA

⁴Department of Medical Physics, University of Wisconsin, Madison, WI 53706, USA

⁵Department of Pathology, University of Illinois at Chicago, Chicago, IL 61801, USA

*gpopescu@illinois.edu

Abstract: New quantitative prognostic markers are needed for improved pancreatic ductal adenocarcinoma (PDAC) prognosis. Second harmonic generation microscopy has been used to show that collagen fiber alignment in PDAC is a negative prognostic factor. In this work, a series of PDAC and normal adjacent tissue (NAT) biopsies were imaged with spatial light interference microscopy (SLIM). Quantitative analysis performed on the biopsy SLIM images show that PDAC fiber structures have lower alignment per unit length, narrower width, and are longer than NAT controls. Importantly, fibrillar collagen in PDAC shows an inverse relationship between survival data and fiber width and length ($p < 0.05$).

© 2020 Optical Society of America under the terms of the [OSA Open Access Publishing Agreement](#)

1. Introduction

Globally, pancreatic cancer is the 12th most common malignancy and the seventh and eighth cause of cancer-related death in men and women, respectively [1]. Its occurrence is growing exponentially, and it is projected to be the second most lethal cancer in the US by 2020 [2]. Approximately 85% of pancreatic malignancies are classified as ductal adenocarcinomas. Pancreatic abnormalities are first confirmed and partially diagnosed through conventional imaging, such as helical computed tomography (CT) [3], contrast-enhanced ultrasound (US) [4], and enhanced magnetic resonance imaging (MRI) [5]. ¹⁸F Fluorodeoxyglucose (FDG) positron emission tomography (PET) has emerged as another method that can detect malignant pancreatic tumors with high sensitivity and specificity [6]. Endoscopic ultrasound - guided fine-needle aspiration biopsy is a reliable technique for classifying tissue of suspected PDAC patients [7,8], though it can produce false negative results [9].

When a suspicious region is indicated by imaging, a tissue biopsy is obtained and prepared for pathology examination with hematoxylin and eosin (H&E) staining. Diagnosis by a pathologist for most cancers is typically highly accurate, although sometimes the subjective human investigation results in inter-observer variability [10]. Prognosis of pancreatic cancer, on the other hand, is far less definitive, having the weakest record among digestive tract cancers [11]. It remains a challenge to ascertain the prospects of recovery after PDAC surgery, as well as the degree of a possible disease regression [12]. After tumoral excisions, more than 75% of PDAC patients have a survival period of less than 5 years. This poor outcome is due to residual lesions left behind by surgery or new metastasis sites, which lead to relapse [13–16].

One of the ongoing deficiencies in PDAC management is the lack of unique detectable qualities that can predict the likely course of the disease. The ability to evaluate the risk of systemic recurrence is vital, as it can help exclude the need for aggressive options, such as vascular resection and reconstruction [17]. PDAC tissue may be readily identified by its pronounced desmoplasia, which is composed of extracellular matrix (ECM) molecules, pancreatic stellate cells (PSCs), as well as other substances, such as cytokines, growth factors, and ECM metabolizing enzymes secreted by the immune system [18]. Recent efforts have demonstrated a strong correlation between stromal microenvironments and patient outcome [19]. It has been found that the extent of organization and symmetry in stromal ECM, particularly in the fibrillar collagen region, plays a critical role in tumor development [20–22]. During cancer progression, the structural integrity of fibrillar collagen is compromised, which leads to tissue strengthening, mechanical interactions [23], a change in metabolites [24] and conditions conducive to cell infiltration [20]. It has recently been shown that PDAC-associated stroma has a markedly aligned configuration, differentiating it from that in benign pancreatic stroma [25]. Furthermore, it was found that stromal collagen alignment has significant potential as a quantifiable PDAC biomarker and is linked to patient survival following surgery [12]. These observations were first made using second-harmonic generation microscopy (SHGM) [26] which is specific to non-centrosymmetric structures, such as collagen fibers. SHGM is a valuable research tool, but might offer limited adoption in the clinic, as it uses bulky and expensive instrumentation and has limited throughput due to raster scanning. The LC-PolScope, an enhanced form of polarized light microscopy [27], has been proposed as a suitable alternative to SHGM for quantitatively imaging fibrillar collagen in tissues, and compared well against SHGM using breast and pancreatic cancer pathology slides [28]. It was shown that the LC-PolScope, a more economic, and simpler system to SHGM, can be used successfully for the quantification of collagen fibers in terms of orientation and alignment [28].

Though it is convenient to use imaging modalities that are specifically sensitive to fibrillar collagen such as SHGM and LC-PolScope, acquiring signal from other tissue features has advantages. For instance, it is constructive to have a comprehensive representation of a biopsy core, cell, ducts and matrix included, for label free diagnosis in surgical pathology. We present that spatial light interference microscopy (SLIM) [29] can be used for this purpose. Recently, it has been shown that similar collagen information can be extracted using SLIM, which is less expensive than SHGM and can be as much as a factor of $\sim 1,000$ faster [30]. Specifically, the collagen fiber orientation in cancerous breast tissue was quantified based on SLIM data [30]. It was shown that the composition, orientation, and alignment of collagen fibers in tumor-adjacent stroma affect tumor growth and metastasis. SLIM is not only sensitive to this fiber orientation but can also detect other components of the tumor biopsy such as tumor cells [31].

In this paper, we use SLIM as a label-free quantitative phase imaging (QPI) technique [29,32], along with an established fiber quantification software approach [33], to explore how collagen fiber properties: alignment per length, width, length, and straightness, relate to malignancies and patient data profiles. Quantitative phase imaging is a method that can measure nanometer scale pathlength changes in a biological specimen [32]. Recent studies show that QPI has clear potential for clinical applications [34–37]. SLIM has previously been used toward the effective diagnosis of breast cancer, which is usually performed through qualitative H&E stained tissue examinations [31]. In addition to its ease of use, efficiency and conduciveness to fiber analysis, the phase images produced by SLIM have also been used to extract various tissue properties, such as scattering length (the average distance between two scattering events) of light scattered by the tissue [38]), optical anisotropy (the average cosine of the scattering angle, found to be reduced in low prostate survival cases [39]), and the spatial fluctuations in refractive index, known as disorder strength [40]. The refractive index of tissue is also accessible in SLIM images, and has previously been used as a marker for prostate malignancies [39]. Furthermore, SLIM uses broadband illumination

light that diminishes speckle artifacts and lends itself well to automated segmentation tools that need both sharp morphological contrast and precise quantitative information [41,42].

In this study, we used our analysis to segment stromal fibers, including collagen, in both PDAC and NAT cores. In contrast to the previous fiber tracking work on SLIM breast tissue images, which only evaluated fiber orientation, here we incorporate four fiber properties and do not require any structural segmentation. Since SLIM is not uniquely sensitive to collagen, an involved process with filters was previously employed to exclude all signals except for the isotropic collagen fibers. Here, however, we leverage the greater number of fiber properties and the drastic morphological dissimilarity in PDAC and NAT cores to dispense with any prior feature extraction. We found significant differences between the filament properties in the two groups and a strong correlation between these and patient survival.

2. Methods

2.1. Tissue microarray (TMA)

The patient cohort consisted of 90 tumor cores and 90 normal adjacent tissue, and one marker core (US Biomax, Inc., #HPan-Adel180Sure-010). From the PDAC group, 62 cases were ductal adenocarcinoma, 20 cases were adenocarcinoma, 4 were adenosquamous carcinoma, 3 were mucinous adenocarcinoma, and 1 was mucinous cystadenoma. Staging levels were I-II, IA, IB, II, IIA, IIB, and IV. The mean overall survival was 23.7 months (range 0-87 months). Sixty of the patients were males and thirty were females. The mean age of the patients was 58.3 years (range 36-83 years).

A board-certified pathologist, who was blinded to clinical grading and all computed data, performed diagnosis on each core using the H&E brightfield images acquired by Aperio ImageScope (Leica Biosystems). The pathologist also indicated the presence of cancer cells and desmoplasia in PDAC histology, as well as healthy acini, veins, ducts, and islets of Langerhans in normal tissue. TMA cores containing necrotic debris or partially missing tissue were all omitted from the final analysis.

2.2. Spatial light interference microscopy (SLIM)

The cores were imaged with spatial light interference microscopy (SLIM) with a resolution of 380 nm using a Nikon Plan-APO 40x/0.95 N.A objective (Fig. 1). SLIM is composed of an inverted phase-contrast microscope with a module attachment at the output (CellVista SLIM Pro, Phi Optics, Inc.). A liquid crystal spatial modulator (SLM) placed at the back focal plane of a Fourier lens (Fig. 1) provides additional phase shifts between the scattered and unscattered light, in increments of $\pi/2$. The pattern projected on the SLM matches exactly the phase ring of the objective pupil. Four intensity images with different phase delays are acquired consecutively, enabling the computation of a phase map [29]. SLIM thereby generates quantitative phase images of the sample that, in turn, provides information on its dry mass density at femtogram precision [43]. All cores were acquired through an automated scan of 1388×1044 -pixel tiles using our integrated custom SLIM software [44]. The scanning procedure took approximately 20 minutes to prepare and, subsequently, each core was covered within 3.3 minutes at a rate of 1 frame/s. The total imaging dimensions amounted to $24 \times 40.2 \text{ mm}^2$, and consisted of 24,120 individual SLIM images, which were stitched to form a mosaic using a python algorithm developed in-house (Fig. 2(A-D)).

2.3. Fiber tracking

Fibrillar structure analysis was performed on SLIM images using the default settings in the CT-FIRE software package, as previously described [22,25,41] (Fig. 2(E)). Alignment per length was calculated according to relative fiber angles in a core, spanning a range of 0.0-1.0 (1.0

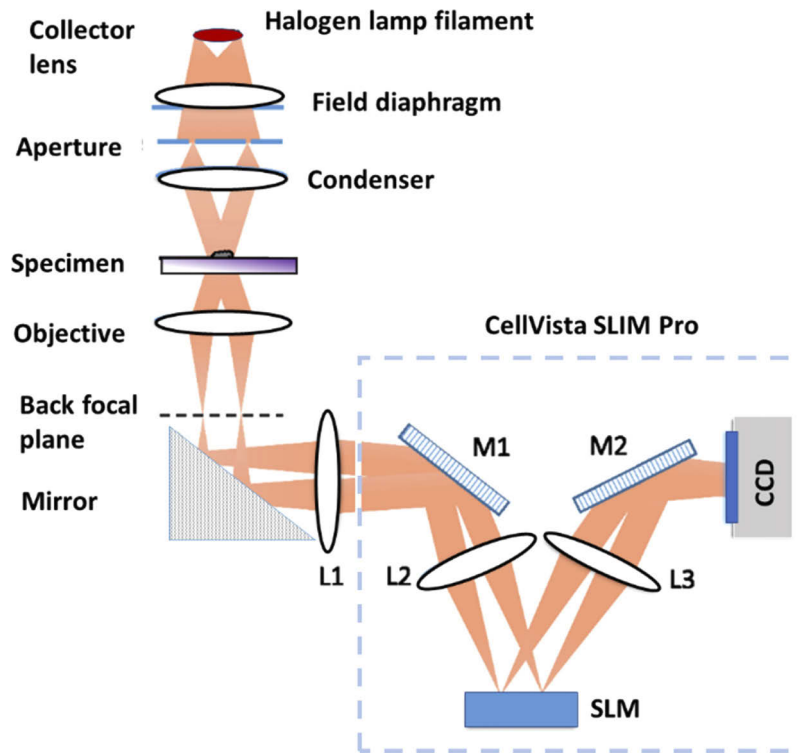


Fig. 1. Schematic for SLIM. The SLIM module is attached to a commercial phase contrast microscope (Nikon Eclipse Ti).

indicates all fibers are parallel), divided by the length of the traced fiber in microns. Length and width were generated initially in pixels and then converted to microns according to a scale calibrated from the 40X Nikon objective. Straightness of fibers was calculated based on tangent angles at successive points tagged on a segmented line (1.0 denotes all fibers are in the same direction). To account for intra-tumoral PDAC heterogeneity on the TMA, all fibers from the cores, amounting to between 4,000 and 5,000 tracking fragments per core, were included in the analysis. We also incorporated the available patient information (grade, stage, gender, age) as covariates in our analysis to estimate their potential clinical application.

2.4. Statistical analysis

Statistical analysis was performed in MATLABTM. The histograms were generated using data retrieved from each fiber. Differences between NAT and PDAC parameters were evaluated using standard deviations for alignment measurements - to account for differences in overall fiber alignment per core - and mean values for the other three properties, with p values obtained from student t-tests. The decision boundary for the principal component analysis (PCA) was obtained using a linear discriminant analysis (LDA) classifier. Survival curves were constructed according to the Kaplan-Meier estimation, with differences calculated according to the Log-rank test. Cutoff values were selected according to the first and last of histogram distributions. The cutoffs for alignment per length were below $0.9^\circ/\mu\text{m}$ and after $1.15^\circ/\mu\text{m}$, for width $0.4\ \mu\text{m}$ and $0.5\ \mu\text{m}$, for straightness 0.919 and 0.928, and for length they were $6.0\ \mu\text{m}$ and $7.9\ \mu\text{m}$. Similar figures were applied to NAT computations. The correlation percentages were computed according to the Pearson's linear correlation coefficient [45].

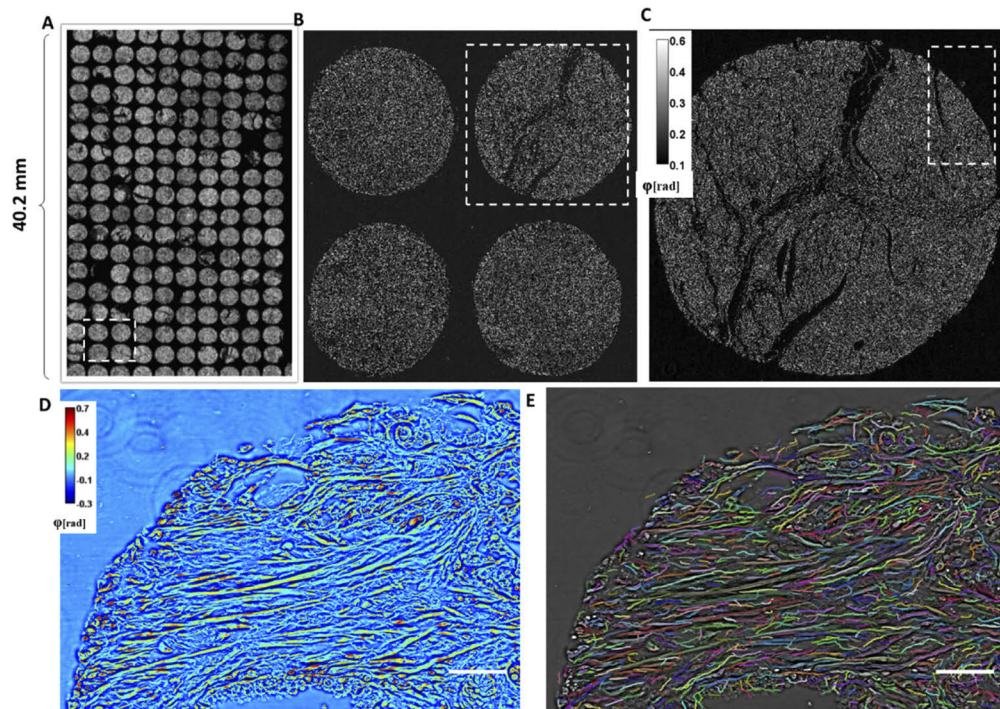


Fig. 2. Stitched SLIM images of the whole TMA slide (Hpan-Ade180Sur-01) (A). SLIM images of PDAC/NAT biopsy cores (scale bar 50 μm) (B-D). Corresponding CT-Fire mapping of fibers for D (E).

3. Results

3.1. Relationship between PDAC and NAT fiber tracking properties

Since the TMA used in this study includes two cores per patient, we were able to image and quantify filamentary details in normal and PDAC regions from the same patient. Upon visual examination, there were evident discrepancies in morphology between cancerous and NAT cores, with notably dense desmoplasia present in PDAC tissue cores. To explore how filament structures relate to malignant characterization, we applied the fiber tracking algorithm on both PDAC and corresponding NAT cores. Since the SLIM signal from NAT cores is nearly as extensive as that from PDAC cores (Fig. 2(B)), there were similar amounts of tracking elements in both core types. The PDAC segments predominantly trace collagen fibers, while those of NAT cores track collagen in addition to the boundaries of acini, veins, ducts, and islets of Langerhans (Fig. 3). Our data show that PDAC cores had fibrillar structures with less alignment per length, narrower width, and greater length and straightness than the corresponding NAT tissue (Fig. 4). In addition to the four fiber properties being significantly different in PDAC compared to normal tissue, considerable distributions in all four fiber features were calculated in each core.

In order to enhance the distinguishing information between core types, quantitative data provided by SLIM was included, along with the four fiber parameters, and dimensionally reduced using PCA. LDA was thereafter performed to distinguish PDAC from NAT cores (Fig. 5(A)). In this case, the mean dry mass density was evaluated for each core according to previously detailed methods using SLIM [43]. A confusion matrix yielded an accuracy of 0.7. Using individual parameters may be more effective however, as ROC curves constructed for each fibrous property (Fig. 5(B)) show that straightness and length have the greatest diagnostic value, with AUCs of 0.83 and 0.82, respectively. There was no significant difference in the four calculated fiber

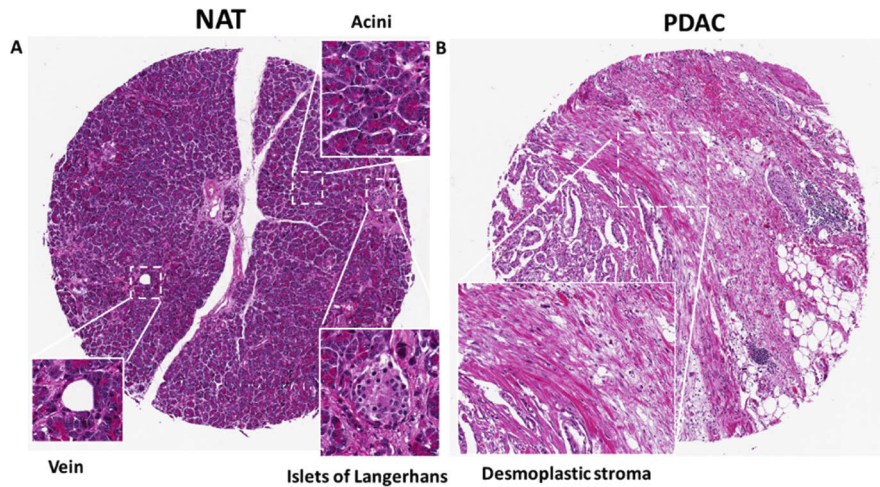


Fig. 3. Stitched brightfield H&E images of whole pancreas biopsy cores (Hpan-Ade180Sur-01). NAT pancreatic core with insets showing zoomed in regions of a duct, acini, a vein, and Islets of Langerhans (A). Corresponding patient PDAC core, with inset showing the characteristic dense desmoplastic stroma (B).

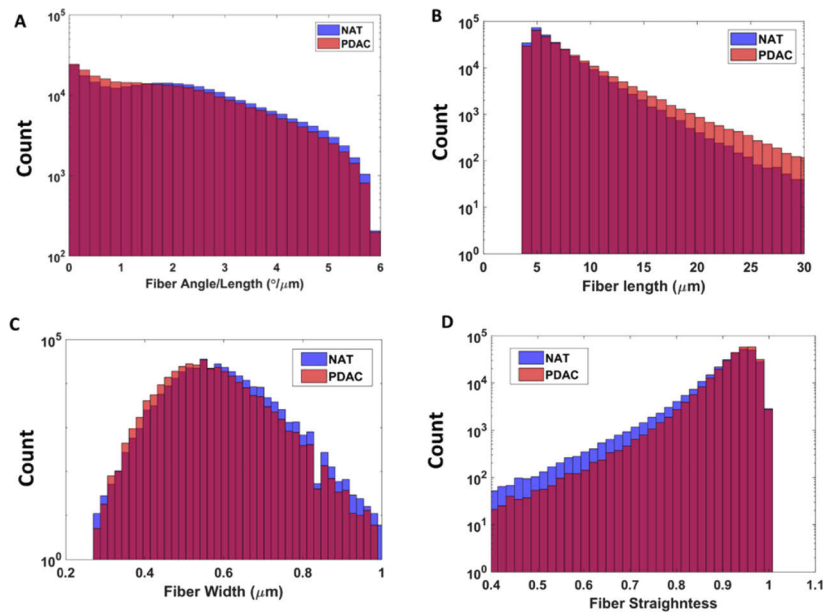


Fig. 4. Histograms (log) of both normal adjacent tissue (NAT) and pancreatic ductal adenocarcinoma (PDAC) fiber angle/length (A), fiber width (B), fiber length (C), and fiber straightness (D) of individual fibers across all cores.

properties between PDAC cores of low and high histological grade. Furthermore, there were no significant correlations found between the other patient characteristics and fiber properties.

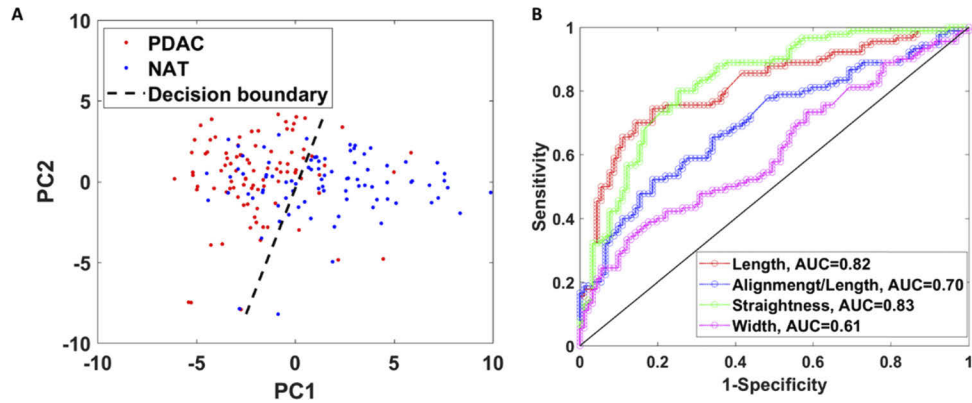


Fig. 5. Plot of first two principal components of mean width, straightness, length, alignment/length fiber parameters, as well as dry mass density for PDAC and NAT cores, with decision boundary (A). ROC curves for discriminating cancerous tissue based on mean fiber length, alignment/length, straightness, and width (B).

3.2. Stromal fibers as marker for patient outcome

PDAC patients with high alignment per length of segmented fibers exhibit significantly reduced survival rates (Fig. 6(A)). Fiber width and length were greater in low survival cases, having associated survival periods of approximately 40 and 60 months, respectively, compared to 80 months for cases with narrower and shorter fiber profiles (Fig. 6(B) and 6(C)). Our results

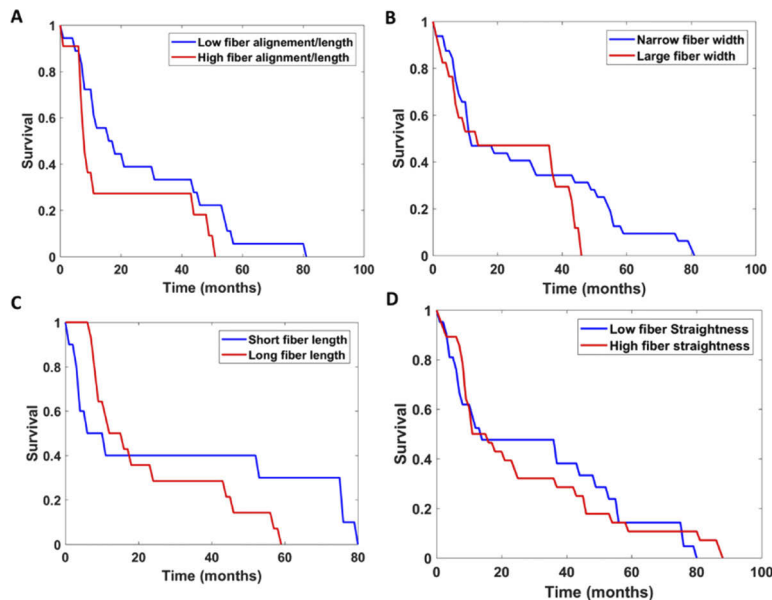


Fig. 6. Kaplan-Meier survival curves for pancreatic ductal adenocarcinoma (PDAC), comparing different grades of fiber alignment/length (A), fiber width (B), fiber length (C), and fiber straightness (D). Log-Rank χ^2 of 50.7 (str), 37.43 (width), 25.7 (al), 50.8 (length).

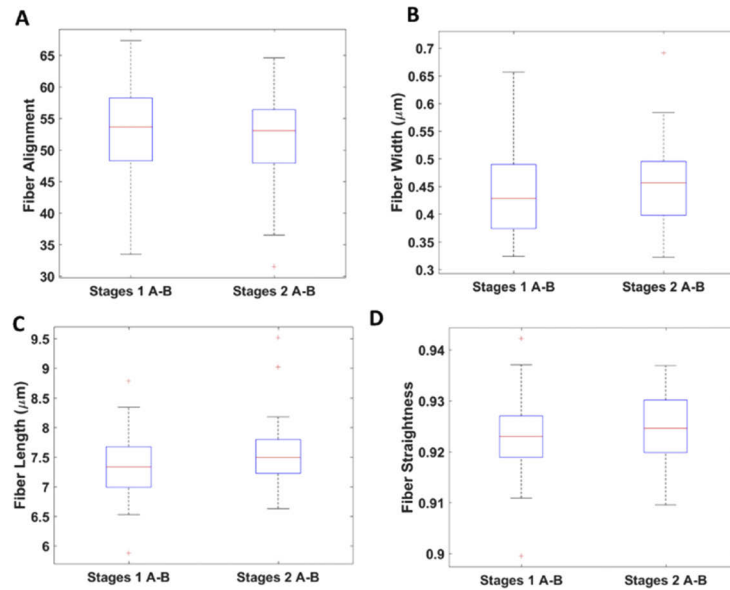


Fig. 7. Difference between stage groups 1 A-B and 2 A-B in pancreatic ductal adenocarcinoma (PDAC) fiber alignment (A), fiber width (B), fiber length (C), and fiber straightness (D). p-values are 0.36, 0.98, 0.184, 0.31, respectively.

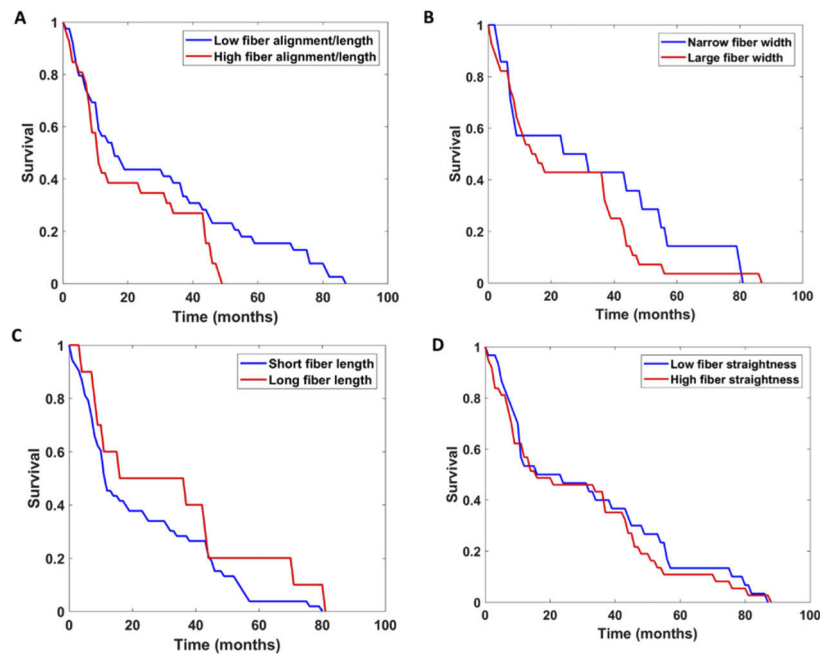


Fig. 8. Kaplan-Meier survival curves for normal adjacent tissue (NAT), comparing different grades of fiber alignment (A), fiber width (B), fiber length (C), and fiber straightness (D). Log-Rank χ^2 of 38.61 (str), 37.43 (width), 21.9 (al), 44.15 (length).

indicate that straightness has less predictive value in survival rates (Fig. 6(D)). The width and length distributions had the greatest standard errors, indicating largest intra-class variability. Surprisingly, the typical disease predictors in tissue, such as tumor stage and grade, were not significant in this patient cohort (Fig. 7). This result is likely due to most of our cases being low stage, mostly IB and IIB.

3.3. Correlation of NAT fiber characteristics with patient data

The NAT tissue of PDAC survival rates did not differ significantly in terms of filament alignment per length, width, length, and straightness (Fig. 8). In the multivariate assessments of NAT cores, comprising stage, grade, age, gender data, no significant differences in the patient cohort were found, which may indicate that NAT cores are not informative of neighboring cancerous tissue.

4. Discussion

The implementation of efficient and sensitive techniques to detect new PDAC markers is vital for effective treatment of this lethal condition. SLIM generates quantitative phase images that inform on useful tissue properties and has high-throughput tissue scanning capability. Using a SLIM-based automated procedure, we show that PDAC cores differ sharply from NAT in terms of segmented properties, including alignment per length, width, length and straightness, enabling rapid and automated diagnostic stratifying potential.

This modality holds promise for clinical application without the need for prior structural processing. SLIM has the advantage over collagen-specific modalities, such as SGHM and LC-PolScope, of providing more inclusionary quantitative information of the cellular microenvironment such as cells and matrix that can be used to detect new prognostic markers. Furthermore, though SLIM is not uniquely sensitive to collagen signals, it holds great promise for diagnostic evaluations on label-free samples such as in surgical pathology application, since there is significant discrepancy in morphology between PDAC and NAT cores, which is fully described in the phase maps. Furthermore, it was found that both larger width and greater length of PDAC collagen fibers are associated with poor patient prognosis. To further explore the value in extracted fiber data, we evaluated the clinical relevance of the variables in patient profiles. The fiber data from NAT cores were evaluated with the same approach. No substantial heterogeneity was observed among patients for NAT, either in survival rates, or stage, grade, gender and age.

These findings establish novel insight on the ECM based morphological aspects of PDAC tissue and its relationship with those of normal adjoining regions. This is an especially important revelation since pancreatic cancer is commonly associated with bleak post-operative prospects.

In summary, we have demonstrated that combining quantitative phase imaging with a fiber tracking algorithm can assist in diagnostic and prognostic evaluations, which may prove beneficial in the clinical setting. Before our method becomes adoptable, further investigations on different tissue samples are needed to consolidate and fine-tune this process. Since SLIM provides a quantitative map of tissue, it lends itself well to the application of machine learning tools to bypass and expedite tedious and expensive histological procedures, as well as refine tissue analysis.

Funding

National Science Foundation (CBET-0939511 STC); National Institutes of Health (CA238191); National Institute of General Medical Sciences (GM129709).

Disclosures

GP has a financial interest in Phi Optics Inc, a company developing quantitative phase imaging instruments.

References

1. L. A. Torre, F. Bray, R. L. Siegel, J. Ferlay, J. Lortet-Tieulent, and A. Jemal, "Global cancer statistics, 2012," *CA Cancer J. Clin.* **65**(2), 87–108 (2015).
2. L. Rahib, B. D. Smith, R. Aizenberg, A. B. Rosenzweig, J. M. Fleshman, and L. M. Matrisian, "Projecting cancer incidence and deaths to 2030: the unexpected burden of thyroid, liver, and pancreas cancers in the United States," *Cancer Res.* **74**(11), 2913–2921 (2014).
3. D. Lu, S. Vedantham, R. M. Krasny, B. Kadell, W. L. Berger, and H. A. Reber, "Two-phase helical CT for pancreatic tumors: pancreatic versus hepatic phase enhancement of tumor, pancreas, and vascular structures," *Radiology* **199**(3), 697–701 (1996).
4. S. Rickes, K. Unkrödt, H. Neye, K. Ocran, and W. Wermke, "Differentiation of pancreatic tumours by conventional ultrasound, unenhanced and echo-enhanced power Doppler sonography," *Scand. J. Gastroenterol.* **37**(11), 1313–1320 (2002).
5. S. J. Diehl, K. J. Lehmann, J. Gaa, S. McGill, V. Hoffmann, and M. Georgi, "MR imaging of pancreatic lesions: comparison of manganese-DPDP and gadolinium chelate," *Invest. Radiol.* **34**(9), 589 (1999).
6. A. Sendler, N. Avril, H. Helmlberger, J. Stollfuß, W. Weber, F. Bengel, M. Schwaiger, J. D. Roder, and J. R. Siewert, "Preoperative evaluation of pancreatic masses with positron emission tomography using 18 F-fluorodeoxyglucose: diagnostic limitations," *World J. Surg.* **24**(9), 1121–1129 (2000).
7. K. J. Chang, P. Nguyen, R. A. Erickson, T. E. Durbin, and K. D. Katz, "The clinical utility of endoscopic ultrasound-guided fine-needle aspiration in the diagnosis and staging of pancreatic carcinoma," *Gastrointest. Endosc.* **45**(5), 387–393 (1997).
8. M. R. Vander Noot, M. A. Eloubeidi III, V. K. Chen, I. Eltoun, D. Jhala, N. Jhala, S. Syed, and D. C. Chheng, "Diagnosis of gastrointestinal tract lesions by endoscopic ultrasound-guided fine-needle aspiration biopsy," *CA Cancer J. Clin.* **102**(3), 157–163 (2004).
9. B. Brand, T. Pfaff, K. Binmoeller, P. Sriram, A. Fritscher-Ravens, W. Knöfel, S. Jäckle, and N. Soehendra, "Endoscopic ultrasound for differential diagnosis of focal pancreatic lesions, confirmed by surgery," *Scand. J. Gastroenterol.* **35**(11), 1221–1228 (2000).
10. R. K. Jain, R. Mehta, R. Dimitrov, L. G. Larsson, P. M. Musto, K. B. Hodges, T. M. Ulbright, E. M. Hattab, N. Agaram, and M. T. Idrees, "Atypical ductal hyperplasia: interobserver and intraobserver variability," *Mod. Pathol.* **24**(7), 917–923 (2011).
11. C. Neuzillet, A. Tijeras-Raballand, P. Bourget, J. Cros, A. Couvelard, A. Sauvanet, M.-P. Vullierme, C. Tournigand, and P. Hammel, "State of the art and future directions of pancreatic ductal adenocarcinoma therapy," *Pharmacol. Ther.* **155**, 80–104 (2015).
12. C. R. Drifka, A. G. Loeffler, K. Mathewson, A. Keikhosravi, J. C. Eickhoff, Y. Liu, S. M. Weber, W. J. Kao, and K. W. Eliceiri, "Highly aligned stromal collagen is a negative prognostic factor following pancreatic ductal adenocarcinoma resection," *Oncotarget* **7**(46), 76197 (2016).
13. K. M. Yamada and E. Cukierman, "Modeling tissue morphogenesis and cancer in 3D," *Cell* **130**(4), 601–610 (2007).
14. A. Richter, M. Niedergethmann, J. W. Sturm, D. Lorenz, S. Post, and M. Trede, "Long-term results of partial pancreaticoduodenectomy for ductal adenocarcinoma of the pancreatic head: 25-year experience," *World J. Surg.* **27**(3), 324–329 (2003).
15. M. Sinn, J. K. Striefler, B. V. Sinn, D. Sallmon, S. Bischoff, J. M. Stieler, U. Pelzer, M. Bahra, P. Neuhaus, and B. Dörken, "Does long-term survival in patients with pancreatic cancer really exist?—Results from the CONKO-001 study," *J. Surg. Oncol.* **108**(6), 398–402 (2013).
16. A. D. Rhim, E. T. Mirek, N. M. Aiello, A. Maitra, J. M. Bailey, F. McAllister, M. Reichert, G. L. Beatty, A. K. Rustgi, and R. H. Vonderheide, "EMT and dissemination precede pancreatic tumor formation," *Cell* **148**(1-2), 349–361 (2012).
17. A. Blackford, O. K. Serrano, C. L. Wolfgang, G. Parmigiani, S. Jones, X. Zhang, D. W. Parsons, J. C.-H. Lin, R. J. Leary, and J. R. Eshleman, "SMAD4 gene mutations are associated with poor prognosis in pancreatic cancer," *Clin. Cancer Res.* **15**(14), 4674–4679 (2009).
18. S. Pandol, M. Edderkaoui, I. Gukovsky, A. Lugea, and A. Gukovskaya, "Desmoplasia of pancreatic ductal adenocarcinoma," *Clin. Gastroenterol. Hepatol.* **7**(11), S44–S47 (2009).
19. K. M. Bever, E. A. Sugar, E. Bigelow, R. Sharma, D. Laheru, C. L. Wolfgang, E. M. Jaffee, R. A. Anders, A. De Jesus-Acosta, and L. Zheng, "The prognostic value of stroma in pancreatic cancer in patients receiving adjuvant therapy," *HPB* **17**(4), 292–298 (2015).
20. P. P. Provenzano, K. W. Eliceiri, J. M. Campbell, D. R. Inman, J. G. White, and P. J. Keely, "Collagen reorganization at the tumor-stromal interface facilitates local invasion," *BMC Med.* **4**(1), 38 (2006).
21. O. Nadiarnykh, R. B. LaComb, M. A. Brewer, and P. J. Campagnola, "Alterations of the extracellular matrix in ovarian cancer studied by Second Harmonic Generation imaging microscopy," *BMC Cancer* **10**(1), 94 (2010).
22. C. J. Hanley, F. Noble, M. Ward, M. Bullock, C. Drifka, M. Mellone, A. Manousopoulou, H. E. Johnston, A. Hayden, and S. Thirdborough, "A subset of myofibroblastic cancer-associated fibroblasts regulate collagen fiber elongation, which is prognostic in multiple cancers," *Oncotarget* **7**(5), 6159 (2016).
23. K. R. Levental, H. Yu, L. Kass, J. N. Lakins, M. Egeblad, J. T. Erler, S. F. Fong, K. Csiszar, A. Giaccia, and W. Weninger, "Matrix crosslinking forces tumor progression by enhancing integrin signaling," *Cell* **139**(5), 891–906 (2009).

24. J. C. Tung, J. M. Barnes, S. R. Desai, C. Sistrunk, M. W. Conklin, P. Schedin, K. W. Eliceiri, P. J. Keely, V. L. Seewaldt, and V. M. Weaver, "Tumor mechanics and metabolic dysfunction," *Free Radical Biol. Med.* **79**, 269–280 (2015).
25. C. R. Drifka, J. Tod, A. G. Loeffler, Y. Liu, G. J. Thomas, K. W. Eliceiri, and W. J. Kao, "Periductal stromal collagen topology of pancreatic ductal adenocarcinoma differs from that of normal and chronic pancreatitis," *Mod. Pathol.* **28**(11), 1470–1480 (2015).
26. P. J. Campagnola and L. M. Loew, "Second-harmonic imaging microscopy for visualizing biomolecular arrays in cells, tissues and organisms," *Nat. Biotechnol.* **21**(11), 1356–1360 (2003).
27. R. Oldenbourg and G. Mei, "New polarized light microscope with precision universal compensator," *J. Microsc.* **180**(2), 140–147 (1995).
28. A. Keikhosravi, Y. Liu, C. Drifka, K. M. Woo, A. Verma, R. Oldenbourg, and K. W. Eliceiri, "Quantification of collagen organization in histopathology samples using liquid crystal based polarization microscopy," *Biomed. Opt. Express* **8**(9), 4243–4256 (2017).
29. Z. Wang, L. Millet, M. Mir, H. Ding, S. Unarunotai, J. Rogers, M. U. Gillette, and G. Popescu, "Spatial light interference microscopy (SLIM)," *Opt. Express* **19**(2), 1016–1026 (2011).
30. H. Majeed, C. Okoro, A. Kajdacsy-Balla, J. K. C. Toussaint, and G. Popescu, "Quantifying collagen fiber orientation in breast cancer using quantitative phase imaging," *J. Biomed. Opt.* **22**(4), 046004 (2017).
31. H. Majeed, M. E. Kandel, K. Han, Z. Luo, V. Macias, K. V. Tangella, A. Balla, and G. Popescu, "Breast cancer diagnosis using spatial light interference microscopy," *J. Biomed. Opt.* **20**(11), 111210 (2015).
32. G. Popescu, *Quantitative phase imaging of cells and tissues*, McGraw Hill Professional (2011).
33. J. S. Bredfeldt, Y. Liu, C. A. Pehlke, M. W. Conklin, J. M. Szulczewski, D. R. Inman, P. J. Keely, R. D. Nowak, T. R. Mackie, and K. W. Eliceiri, "Computational segmentation of collagen fibers from second-harmonic generation images of breast cancer," *J. Biomed. Opt.* **19**(1), 016007 (2014).
34. C. Hu and G. Popescu, "Quantitative Phase Imaging (QPI) in Neuroscience," *IEEE J. Sel. Top. Quantum Electron.* **25**(1), 1–9 (2019).
35. M. Lee, E. Lee, J. Jung, H. Yu, K. Kim, J. Yoon, S. Lee, Y. Jeong, and Y. Park, "Label-free optical quantification of structural alterations in Alzheimer's disease," *Sci. Rep.* **6**(1), 31034 (2016).
36. P. Wang, R. Bista, R. Bhargava, R. E. Brand, and Y. Liu, "Spatial-domain low-coherence quantitative phase microscopy for cancer diagnosis," *Opt. Lett.* **35**(17), 2840–2842 (2010).
37. T. H. Nguyen, S. Sridharan, V. Macias, A. Kajdacsy-Balla, J. Melamed, M. N. Do, and G. Popescu, "Automatic Gleason grading of prostate cancer using quantitative phase imaging and machine learning," *J. Biomed. Opt.* **22**(3), 036015 (2017).
38. H. Majeed, S. Sridharan, M. Mir, L. Ma, E. Min, W. Jung, and G. Popescu, "Quantitative phase imaging for medical diagnosis," *J. Biophotonics* **10**(2), 177–205 (2017).
39. S. Sridharan, V. Macias, K. Tangella, A. Kajdacsy-Balla, and G. Popescu, "Prediction of prostate cancer recurrence using quantitative phase imaging," *Sci. Rep.* **5**(1), 9976 (2015).
40. M. Takabayashi, H. Majeed, A. Kajdacsy-Balla, and G. Popescu, "Disorder strength measured by quantitative phase imaging as intrinsic cancer marker in fixed tissue biopsies," *PLoS One* **13**(3), e0194320 (2018).
41. C. Hu, M. Santi, O. Adelaja, A. Kajdacsy-Balla, G. Popescu, and W. Kobak, "Imaging collagen properties in the uterosacral ligaments of women with pelvic organ prolapse using spatial light interference microscopy (SLIM)," *Front. Phys.* **7**, 72 (2019).
42. H. S. Park, M. Rinehart, K. A. Walzer, J. T. A. Chi, and A. Wax, "Automated Detection of *P. falciparum* Using Machine Learning Algorithms with Quantitative Phase Images of Unstained Cells," *PLoS One* **11**(9), e0163045 (2016).
43. G. Popescu, Y. Park, N. Lue, C. Best-Popescu, L. Deflores, R. R. Dasari, M. S. Feld, and K. Badizadegan, "Optical imaging of cell mass and growth dynamics," *Am. J. Physiol. Cell Physiol.* **295**(2), C538–C544 (2008).
44. M. E. Kandel, S. Sridharan, J. Liang, Z. Luo, K. Han, V. Macias, A. Shah, R. Patel, K. Tangella, and A. Kajdacsy-Balla, "Label-free tissue scanner for colorectal cancer screening," *J. Biomed. Opt.* **22**(6), 066016 (2017).
45. M. M. Mukaka, "A guide to appropriate use of correlation coefficient in medical research," *Malawi Med. J.* **24**(3), 69–71 (2012).